Colloids and Surfaces B: Biointerfaces 248 (2025) 114476

Contents lists available at ScienceDirect

Colloids and Surfaces B: Biointerfaces

journal homepage: www.elsevier.com/locate/colsurfb

Investigation of bacterial nanocellulose/calcium phosphates-based composite containing cerium for bone repair

Ricardo Barbosa Sousa [a,b,*], Alessandra Cristina Dametto [c], Gabriela Fontana de Mesquita [d], Pedro Henrique Ricardo [d], Júlia Venturini Helaehil [d,e], Santiago Medina-Carrasco [f], Josy Anteveli Osajima Furtini [b], Guilherme Ferreira Caetano [d,e,g], Hernane S. Barud [h], Edson C. Silva-Filho [b]

[a] Federal Institute of Education, Science, and Technology of Tocantins, Campus Araguaina, 56, Amazonas Avenue, Araguaina, TO 77.824-838, Brazil
[b] Interdisciplinar Laboratory of Advanced Materials, LIMAV, UFPI, Teresina, PI, Brazil
[c] BioSmart Nanotechnology, Araraquara, SP, Brazil
[d] University Center of Hermínio Ometto Foundation/FHO, Araras, SP, Brazil
[e] Division of Dermatology, Department of Internal Medicine, São Paulo University (USP), Ribeirão Preto Medical School, Ribeirão Preto, SP, Brazil
[f] X-Ray Laboratory (CITIUS), University of Seville, Seville, Spain
[g] Graduate Program of Orthodontics, University Center of Hermínio Ometto Foundation (FHO), Araras, SP, Brazil
[h] Biopolymers and Biomaterials Laboratory (BioPolMat), Araraquara, SP, Brazil

ARTICLE INFO

Keywords:
Bone regeneration
Lanthanides
Polysaccharides

ABSTRACT

Bacterial nanocellulose (BNC) has attracted considerable attention in the field of biomedical engineering due to its potential for use in bone regeneration applications. The present study investigates the *in vitro* and *in vivo* efficacy of bacterial nanocellulose (BNC) combined with calcium and cerium ions (BNC-Ce:CaP) in bone regeneration applications. XRD analysis confirmed the presence of monetite and hydroxyapatite phases in BNC-CaP, while BNC-Ce:CaP revealed an additional brushite phase. Based on XPS analysis, cerium (III) is found in BNC-Ce:CaP at a concentration of 4.14 % (mol/mol). BNC revealed ultrafine 3D nanofibers with diameters ranging from 20.8 to 53.0 nm, while BNC-Ce:CaP composite, containing cerium, exhibited urchin-like structures with diameters around 1 μm and BNC-CaP composite presented phosphates covering the fiber surfaces, leading to significant thickness increases and pleat formation (70–180 nm). The composite materials demonstrated insignificant cytotoxicity. The results performed by histomorphometric analysis demonstrated that the BNC-Ce:CaP composites showed superior mineralized tissue formation after 60 days. Gene expression revealed a reduction in the inflammatory response and an increase in the expression of osteogenic markers, such as Bmp-2 and Osterix, in addition to an increase in the expression of angiogenic genes, such as Vegf. These findings highlight the potential of BNC-Ce:CaP composites as effective barriers to promote bone regeneration.

1. Introduction

Bacterial nanocellulose (BNC) is an alternative material biosynthesized extracellularly mainly by Gram-negative bacteria, such as *Komagataeibacter*, which is the most prominent and efficient BNC producer, industrially explored [1,2]. Compared to plant cellulose, BNC has various advantages, starting with the purification process, which is sustainable and generates less waste [3].

Moreover, BNC demonstrates exceptional mechanical and structural properties when compared to plant cellulose. These include high flexibility, remarkable water uptake capacity (up to 400 times its dry weight), hydrophilicity, elevated purity and crystallinity, ultrafine fiber network, high porosity, substantial tensile strength, and ability to be molded into various structures [2,4–7]. While plant-based cellulose fibers are renewable, abundant, cost-effective, and biodegradable, they are often associated with non-biodegradable molecules such as lignin and hemicellulose [8].

Despite its exceptional properties, BNC (bacterial nanocellulose)

* Corresponding author at: Federal Institute of Education, Science, and Technology of Tocantins, Campus Araguaina, 56, Amazonas Avenue, Araguaina, TO 77.824-838, Brazil.
E-mail address: ricardo.sousa@ifto.edu.br (R.B. Sousa).

https://doi.org/10.1016/j.colsurfb.2024.114476
Received 19 October 2024; Received in revised form 15 December 2024; Accepted 23 December 2024
Available online 24 December 2024

alone may not meet all the necessary requirements for certain biomedical applications, often requiring chemical modification or combination with other materials, such as the incorporation of cerium ions, which not only improve the biocompatibility of the composites but also play a key role in modulating the inflammatory response and promoting bone regeneration. The addition of cerium to BNC-CaP composites is a significant advantage, as it enhances osteogenic and angiogenic properties, offering new perspectives for the development of biomaterials in tissue engineering [9–12].

One class of materials that has received significant attention is BNC-calcium phosphate-based composites, mainly due to the interfacial phenomena involved, which result in increased desirable biomechanical properties. BNC containing hydroxyapatite (HAp) is particularly interesting, as HAp closely resembles the apatite found in bones and teeth, having exceptional properties, such as biocompatibility, HAp is highly compatible with biological tissues, this means that it does not cause adverse or inflammatory reactions, presents also bioactivity and can interact with biological tissues to promote osteoconduction, in addition to having mechanical properties such as fracture resistance and toughness. Organic-inorganic hybrids, such as bacterial nanocellulose/calcium phosphates, are considered highly promising for manufacturing bone implants [13]. This is due to the advantageous combination of properties of the organic matrix (BNC), which offers ease of processing, high flexibility and low density, with beneficial attributes of the inorganic phase (apatite), including high thermal stability characteristic of ceramic materials [14].

Furthermore, researchers have delved into understanding the impact of metal ion clusters within calcium phosphates on bone repair mechanisms. Among these ions, cerium ions (Ce^{3+}/Ce^{4+}) have garnered significant interest [15–18]. According to Santos et al. [19] cerium ions, when present in small amounts in calcium phosphates, can extend the biocidal action of drugs while enhancing crucial biological properties such as biocompatibility and material reabsorption in tissue. Ren et al. [20] highlighted cerium's role in regulating the migration and osteogenic differentiation of bone marrow stromal cells. Their study evaluated membranes containing cerium oxide nanoparticles (CeO_2 NPs) at various concentrations, assessing properties like antibacterial activity, biocompatibility, and hemocompatibility. The results demonstrated the material's angiogenic potential and effectiveness in inhibiting pathogens. *In vitro* findings also suggested that CeO_2 NPs promote osteoblast proliferation, differentiation, mineralization, and the osteogenic differentiation of human periodontal ligament stem cells. Notably, cerium naturally occurs in healthy bone tissue and accumulates with age [20].

The presence of cerium in bacterial nanocellulose membranes may also contribute positively to reducing oxidative stress, making it beneficial for applications in treating inflammatory and chronic lesions. This characteristic has led to the use of cerium nanoparticles in promoting bone tissue regeneration as well as in the therapy of drug-induced liver damage and inflammatory bowel diseases [21–26].

The aim of this study is to prepare, characterize, and assess the bone regeneration potential of bacterial nanocellulose (BNC), bacterial nanocellulose/calcium phosphate (BNC-CaP) composites, and bacterial nanocellulose/calcium phosphate composites containing cerium (BNC-Ce:CaP).

2. Experimental

2.1. Materials

BNC membranes used in this work were cultivated at the Biopolymers and Biomaterials Laboratory (BioPolMat) of the University of Araraquara, Araraquara - SP, from the strain *Komagataeibacter rhaeticus* and purified in an alkaline medium (NaOH 1.0 mol L^{-1}) and under heating at 70°C. Calcium chloride dihydrate, $CaCl_2{\cdot}2H_2O$ (97 %), was purchased from Dinâmica Brazil, dibasic sodium phosphate dihydrate, Na_2HPO_4 (98 %), was purchased from Synth Brazil and cerium(III) nitrate hexahydrate, $Ce(NO_3)_3{\cdot}6H_2O$ (99 %), was purchased from Sigma-Aldrich. All chemical reagents were used without previous purification.

2.2. Preparation of the BNC-based composites

Pristine wet bacterial nanocellulose were washed with distilled water and cut into dimensions of approximately 3 cm× 3 cm. Then, these materials were separated into three groups in order to prepare bacterial nanocellulose (BNC), bacterial nanocellulose/calcium phosphate (BNC-CaP) composites and bacterial nanocellulose/calcium phosphate composites containing cerium (BNC-Ce:CaP), as described below.

The BNC-CaP group was prepared in triplicate using the successive immersion method as described by Hutchens et al. [27] and Sousa et al. [8]. In brief, BNC membranes underwent six alternate immersion cycles in solutions of $CaCl_2{\cdot}2H_2O$ at 0.5 mol L^{-1} and Na_2HPO_4 at 0.3 mol L^{-1}. This amount of cycles was chosen once according to Hutchens et al. [27], hydroxyapatite phases increase with more alternate cycles. The BNC-Ce:CaP group was prepared in triplicate using the alternating immersion method of the BNC membranes according to methodology previously described by Sousa et al. [8], without calcination step. After obtaining the composites, all the samples were frozen at −80 °C for 24 hours and then lyophilized using a Liobras L101 lyophilizer (Brazil) at −50 °C for 72 hours.

2.3. Characterization of the BNC-based composites

To characterize the morphology of the samples, scanning electron microscopy (SEM) was used in an electronic microscope JEOL model JSM7500F. The SEM images were treated using the free software *ImageJ* version 1.59e, in order to measure the average sizes of the formed structures. The X-ray photoelectron spectroscopy (XPS) spectra were recorded on a Physical Electronic spectrometer (PHI Versa Probe II) using monochromatic Al K radiation (52.8 W, 15 kV, 1486.6 eV) and a dual-beam charge neutralizer for analyzing the core-level signals of the elements of interest with a hemispherical multichannel detector. The samples were analyzed with a constant pass energy value at 29.35 eV and a beam diameter of 100 μm. The energy scale was calibrated using Cu $2p_{3/2}$, Ag $3d_{5/2}$, and Au 4 $f_{7/2}$ photoelectron lines at 932.7, 368.2, and 83.95 eV, respectively. The spectra obtained were analyzed using PHI SmartSoft software and processed using the MultiPak 9.6.0.15 package. The binding energy values were referenced to C 1 s signal at 284.5 eV. Shirley-type background and Gauss–Lorentz curves were used to determine the binding energies. Atomic concentration percentages of the characteristic elements were determined considering the corresponding area sensitivity factor for the different measured spectral regions. Thermogravimetric analysis were carried out in order to evaluate the thermal stability of the samples in an SDT Q600 - TA Instruments, using a synthetic air atmosphere, heating flow of 10 °C min^{-1}, in the temperature range between 30 and 600 °C. In order to carry out a qualitative evaluation of the crystalline phases present in the samples, X-ray diffraction analysis were carried out in a Shimadzu XRD 6000 diffractometer with a nickel filter and Cu Kα radiation (λ = 1.5406 Å), with 2θ in the range between 10 and 60°, scan rate of 2° min^{-1} and average exposure time of approximately 40 min. Diffraction data were studied using *P'Analytical's X'Pert HighScore Plus* software (v. 2.0.1).

20.8 The analyzes were carried out in a *Bruker* VERTEX 70 spectrophotometer, DLaTGS detector, using the ATR method, in the reading range between 4000 and 400 cm^{-1}.

2.4. Cell viability

Cell viability was evaluated using the MTT method following the guidelines of the ISO 10993-5 protocol [28]. Normal human fibroblasts (GM07492) were cultured in Dulbecco's Modified Eagle's Minimal

Essential Medium (DMEM) supplemented with fetal bovine serum (FBS), antibiotics (penicillin 10,000 U mL^{-1} and streptomycin 10 mg mL^{-1} - Sigma), and antifungal agent (amphotericin B 25 μg mL^{-1} – Sigma). The cells were seeded in 96-well plates, with a cell concentration of 1×10^4 cells per well, exposed to 100 μL biomaterial extracts, and then incubated for 24 h. Subsequently, MTT reagent [3-(4,5-dimethyl-2-thiazolyl)-2,5-diphenyl-2H-tetrazolium bromide] was added, and after further incubation, formazan crystals were dissolved. Optical density was measured at 570 nm, with cell viability calculated relative to a negative control (100 % viability), consisting of a mixture of DMEM + FBS + antibiotics + antifungal and a positive control (0 % viability) consisting of DMEM+ SBF + DMSO 30 % (v/v). The optical density (OD) values were measured using a spectrophotometer and converted into cell viability relative to the negative control, according to Eq. (1):

$$OD(\%) = \frac{Abs\ treated\ cells}{Abs\ negative\ control}\ x\ \ 100 \quad (1)$$

where Abs, corresponds to the absorbance recorded at 570 nm.

2.5. Animal model

It is important to highlight that all activities involving animals at Fundação Hermínio Ometto are regulated by various ethical and legal guidelines established by the National Council for Animal Experimentation Control (CONCEA). The practices adopted adhere to the principles of the 3Rs as described by William Russell and Rex Burch in "The Principles of Humane Experimental Technique". Additionally, it is relevant to mention that the development of the current project was approved by the Ethics Committee on Animal Use, according to opinion N. 088/2018.

54 male Wistar rats (3 months old, 300 g) from the Animal Experimentation Center 'Prof. Dr. Luiz Edmundo de Magalhães' at the University Center of Hermínio Ometto Foundation (FHO) were randomly selected. Temperature and humidity were monitored and kept constant throughout the experiment, along with a 12-hour light/dark cycle to ensure appropriate lighting conditions. Additionally, the animals had *ad libitum* access to food and water, ensuring the availability of necessary nutritional and hydration resources for their well-being.

2.5.1. Surgical procedure

Before the surgical procedure, the animals were anesthetized with a combination of Ketamine (30 mg kg^{-1}) and Xylazine (10 mg kg^{-1}) administered intraperitoneally. Once anesthetized, trichotomy was performed, and after careful disinfection with 70 % alcohol, an incision was made with a scalpel to expose the calvarial bone. Using an Osteo 1 type tip (Helse Dental Technology, Santa Rosa de Viterbo, SP, Brazil) attached to a handpiece of a Piezoelectric Dental Ultrasonic System (Olsen, Palhoça, SC, Brazil) with a power of 20 W and a frequency of 28 Hz, osteotomy was performed to create a critical defect of 25 mm^2 in the occipital region of the calvaria, with constant irrigation using sterile physiological saline solution (NaCl 0.9 %). The animals were divided into the following groups: BNC (bacterial nanocellulose), BNC-CaP (bacterial nanocellulose/calcium phosphates composite), and BNC-Ce:CaP (bacterial nanocellulose/calcium phosphates containing cerium ions). The membranes were placed over the bone defect, and subsequently, sutures were performed to close the incision. Finally, the animals received an analgesic combination of tramadol (1 mg kg^{-1}) and sodium dipyrone (50 mg mL^{-1}) intraperitoneally and orally, respectively, every 12 hours for three days.

2.5.2. Sample collection

For the collection of samples from the occipital calvaria region, after the 30th and 60th day of the surgical procedure, the animals were euthanized under anesthesia depth doubled compared to that used during surgery, followed by cervical dislocation. To avoid collecting adjacent tissue to the lesion, only the injured tissue along with the membrane was removed. Three samples were collected from each group at each experimental time point for histomorphometric analysis, totaling 18 samples. Histological samples were immediately fixed in 10 % formaldehyde, pH 7.4, for 48 hours. The remaining 36 samples, six per group per experimental time point, were immediately frozen at −80 °C for future molecular evaluations.

2.5.3. Histomorphometry

The damaged bone tissue samples were fixed in 10 % formaldehyde, pH 7.4, for 48 h underwent the decalcification process in a buffered solution containing 50 % formic acid for approximately two months, with periodic solution changes to prevent saturation. Subsequently, the specimens were subjected to paraffin embedding procedures (Histosec®-Merck), and semi-serial cross-sections with a thickness of 4.0 μm were made. Masson's Trichrome staining was then performed to quantify the mineralized tissue, osteoid tissue, dense connective tissue, and loose connective tissue, according to specialists on connective tissue and following strict critical evaluation [29].

Sample images were captured using a Leica DM2000 microscope at the Micromorphology Laboratory of the University Center of the Hermínio Ometto Foundation/FHO with Leica Application Suite-Las (version 3.30) at a 200× magnification in bright-field mode and analyzed in *ImageJ* 1.46r software. The area of tissue showing mineralization was outlined and measured to obtain values for mineralized tissue, while the remaining tissue was classified as osteoid matrix, dense connective tissue, and loose connective tissue.

2.5.4. Evaluation of the expression of pro-inflammatory, anti-inflammatory, and osteogenic genes (RT-qPCR)

The defective bone tissue samples collected at 30 and 60-day time points were pulverized in liquid nitrogen. Subsequently, 1 mL of TRIzol (Invitrogen, catalog number 15596026) was added to perform cellular lysis with the assistance of a homogenizer (Polytron System PT 1200E), following the manufacturer's instructions. The concentration and quality of RNA samples were measured and cDNA was synthesized from 1.5 μg of total RNA using the High Capacity kit (Thermo Fisher Scientific, catalog number 4374966), following the manufacturer's instructions. TaqMan assays (Table S1) were conducted in duplicate using the TaqMan Gene Expression Master Mix (Applied Biosystems, catalog number 4369016). The entire RT-qPCR procedure was conducted on the QuantStudio 3 Real-Time PCR Systems platform (Thermo Fisher). The thermal cycling conditions used were 95°C for 10 min, followed by 45 cycles of 95°C for 15 seconds and 60 °C for 1 min. The reference gene Gapdh was tested and validated using the Best-Keeper software and used as a normalizer. The results were expressed using the $2^{-\Delta\Delta CT}$ method.

2.5.5. Statistical analysis

The obtained data were subjected to the Shapiro-Wilk normality test. Values that fell within the normality curve were subjected to one-way ANOVA and Bonferroni post-test, while data that did not conform to the normality curve underwent the Kruskal-Wallis test with Dunn's post-test. Differences were considered significant when the p-value was less than 5 % (α=0.05). Statistical tests and the production of graphs were performed using GraphPad Prism 8.0 software (USA). Values are presented as mean/standard error of the mean. The bars above the columns represent statistical differences between the groups, considering the levels of significance of *$p < 0.05$, **$p < 0.01$, ***$p < 0.001$).

3. Results and discussion

3.1. Characterization

The morphological characteristics of the lyophilized bacterial cellulose (BNC) fiber, as well as the BNC-CaP and BNC-Ce:CaP composites are illustrated in the scanning electronic microscopy images in Fig. 1.

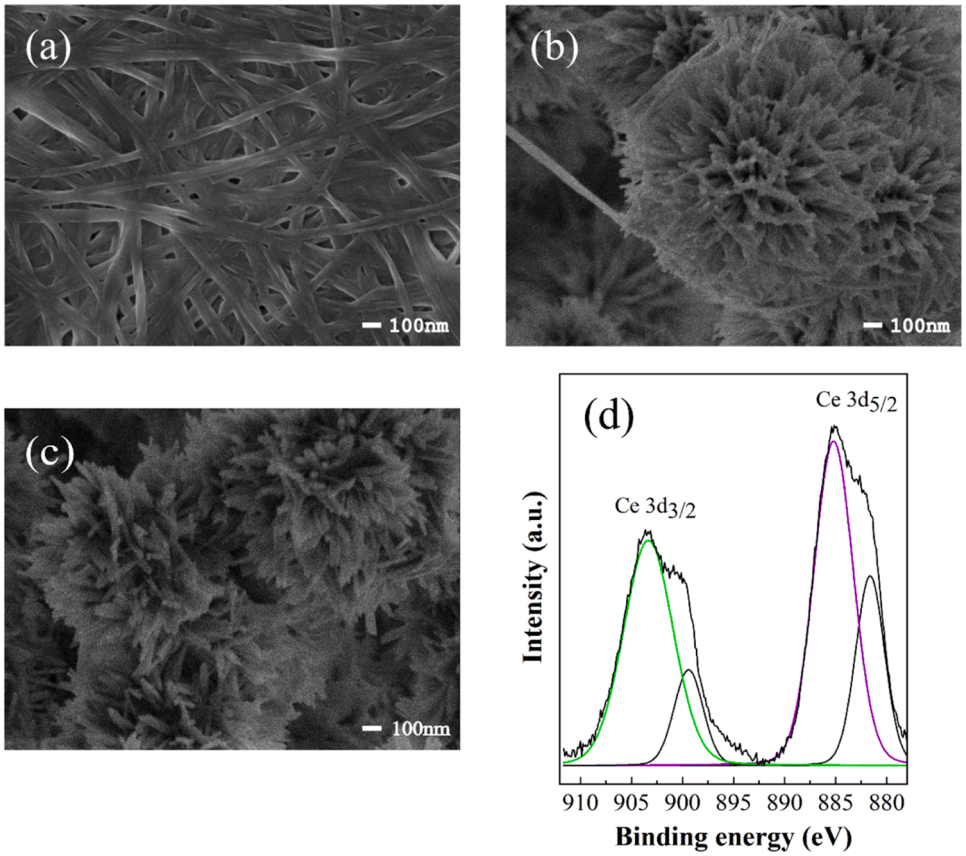

Fig. 1. Surface FEG-SEM images at 50,000× magnification for BNC (a), BNC-Ce:CaP (b) and BNC-CaP (c) and X-ray photoemission spectra of BNC-Ce:CaP (d).

BNC, comprising ultrafine 3D nanofibers with diameters ranging from 20.8 to 53.0 nm (Fig. 1a), has been previously described by various authors, including Saska et al. [30] and Busuioc et al. [31] as an optimal structure for calcium phosphate growth, requiring freeze-drying to preserve its architecture.The BNC-Ce:CaP composite (Fig. 1b), containing 5 % (mol/mol) cerium, exhibits urchin-like structures with diameters around 1 μm and nanometer-scale spines (20–45 nm). In the BNC-CaP composite (Fig. 1c), partially formed urchin-like structures were also observed, with diameter around 1.5 μm [32–39]. Cerium presence possibly influences the formation of urchin-like structures, as seen in other studies like Wei et al. [40] who produced hierarchical ceria urchin-like structures using solvothermal methods followed by calcination.

X-ray photoelectron spectroscopy (XPS) was performed to confirm the chemical composition and the chemical state of cerium in BNC-Ce:CaP biomaterial (Fig. 1d). Through XPS, peaks at binding energy (B.E.) were decomposed into components centered at approximately of 346.9 eV and 350.5 eV (Ca 2p), 133.0 eV (P 2p), 530.7 eV (O 1s), which reveals the presence of the elements Ca, P and O that composes ceramic fraction of BNC-CaP and BNC-Ce:CaP materials (Fig. S1). Furthermore, the detection of Ce 3d photoemission signal in the XPS survey spectrum corroborated with the signals for Ce (III) cations for BNC-Ce:CaP. Although the observed complexity of the Ce 3d XPS spectrum, mainly due to the hybridization between Ce 4f and O 2p levels, four main peaks were observed corresponding to Ce(III) [41]. Those peaks appeared between 880 and 905 eV and are associated with the pairs of spin-orbit doublets ($3d_{5/2}$ and $3d_{3/2}$) at B.E. of 903.43, 899.40, 885.23, 881.46 eV of the Ce^{3+} species (Fig. 1d). Additionally, there was no evidence of the presence of Ce(IV) in this sample, once there are no peaks above 912 eV. In addition, the inter-component energy separation (ΔE), which results from the spin-orbit coupling, for the Ce 3d orbital is 18.2 eV, value close to the referred by [42]. The Ca/P ratio of these materials was also calculated using data provided by the XPS survey spectra. The results showed that the Ca/P ratio for BNC-CaP was 0.95. The (Ca+Ce)/P ratio, which considers the total cation quantification, was 0.71 for BNC-Ce:CaP. So, those calcium phosphates can be considered calcium deficient. The atomic concentration of cerium was 4.14 % in the BNC-Ce-CaP composite.

Fig. 2a–c shows the thermogravimetric curves (TG-DTG) for pristine BNC and BNC-CaP and BNC-Ce:CaP composites. For BNC membranes, two thermal events are observed (Fig. 2a): the first, very discrete, corresponds to a weight loss of 1.70 % and extends from approximately 42.8 °C to 101 °C, and is attributed to the loss of water and water molecules linked by hydrogen bonds during this initial stage. The second and main event corresponds to the degradation of bacterial cellulose, in which depolymerization, dehydration and decomposition of glycosidic units are involved, which results in the formation of carbonaceous residues [43]. This corresponds to a loss of 83.90 % in mass, centered at around 357 °C.

For the BNC-CaP and BNC-Ce:CaP composites, three events of weight loss were observed: the two-stage water loss behavior was related to the elimination of physisorbed water. The presence of calcium phosphates in the composites contributes to the increase in the water content adsorbed on the surface of the composites and this is reflected in the mass losses in water of 4.14 % and 3.05 %, as seen in Fig. 2b and c, respectively. The dehydration process of the composites occurs in more than one stage that extends up to around 300 °C [31], when the most important phenomenon begins: the combustion of bacterial cellulose. It can be seen that, for the composites, the presence of the ceramic fraction had a significant contribution to reduce the thermal stability of bacterial cellulose. According to Saska et al. [30], this behavior may be associated with the breaking of hydrogen bonds and, consequently, a reduction in BNC crystallinity. In fact, the reduction in crystallinity leads to lower maximum temperature values. The fourth event, as suggested by

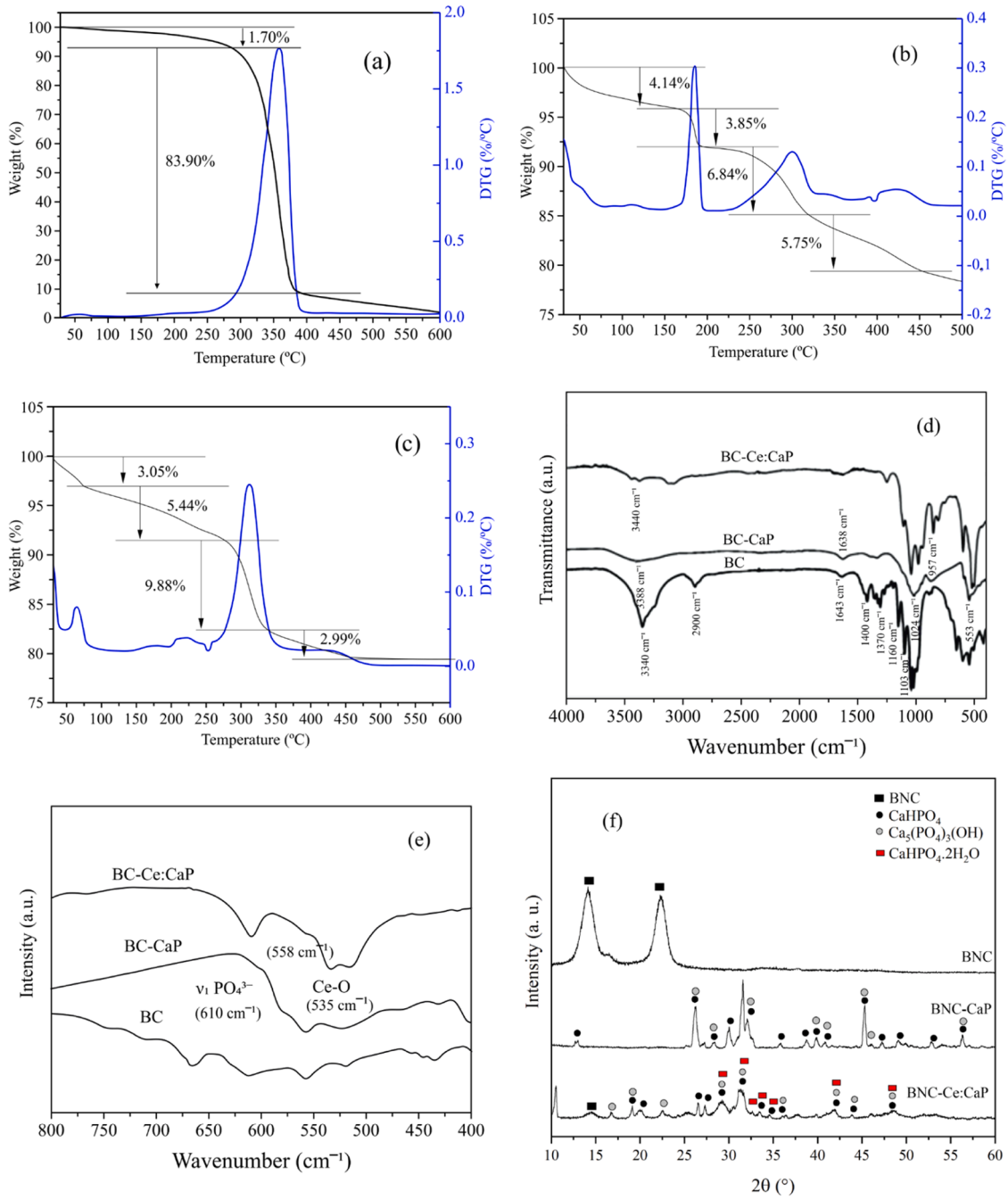

Fig. 2. TG/DTG of each sample: (a) Freeze-dried bacterial cellulose (BNC), (b) Bacterial cellulose/calcium phosphate composite (BNC-CaP), (c) Bacterial nanocellulose/calcium phosphate composite with 5 % (mol/mol) cerium (BNC-Ce:CaP). FTIR spectra for BNC, BNC-CaP and BNC-Ce:CaP (d) and their magnification for 800–400 cm^{-1} region (e). XRD patterns of BNC, BNC-CaP and BNC-Ce:CaP.

Busuioc and collaborators [31], can be attributed to the loss of CO_2 that is integrated in the form of CO_3^{2-} ions, from the atmospheric air in previous stages.

Fig. 2d presents the vibrational spectra in the infrared region for freeze-dried BNC and for the composites (BNC-CaP and BNC-Ce:CaP). For the BNC membranes, the following spectrum band assignments are characteristic, as shown in Fig. 2d: 3340 cm^{-1} -OH stretching, around 2900 cm^{-1} from asymmetric/symmetric stretch of CH_2 from the alkyl group, asymmetric stretching of CH_2 1643 cm^{-1}- angular deformation of the water molecules that are adsorbed on the cellulose structure, at around 1400 cm^{-1} -OH deformation, 1370 cm^{-1} - CH_3 deformation, in the range between 1320 and 1030 cm^{-1} - CO deformation [44,45].

Fig. 2d also presents the IR spectrum of BNC-CaP, where the occurrence of the following bands is identified: 3388 cm^{-1} - OH stretching characteristic, 1638 cm^{-1} referring to the angular deformation of the adsorbed water molecules in the composite, 1345 cm^{-1}, characteristic of deformation C-OH in the plane, 1024 cm^{-1}, characteristic of the asymmetric stretching of the PO_4^{3-} groups, 957 cm^{-1} symmetric stretching of the PO_4^{3-} groups in HPO_4^{2-} and 553 cm^{-1} in asymmetric deformation of PO_4^{3-} [46–48]. Few bands for cellulose were observed for BNC-CaP, likely due to the application of the successive immersion method, which produced layers of calcium phosphates on the bacterial nanocellulose. This may hinder the access of the evanescent wave generated by total internal reflection in the ATR crystal.

Regarding the BNC:Ce-CaP composite, the IR spectra presented in Fig. 2d and e demonstrate some common bands. Notably, the occurrence

of bands at around 3444 cm^{-1} is characteristic of the stretching of the -OH groups of cellulose and those present in calcium phosphates. At around 1634 cm^{-1}, a band occurs relating to the -OH deformation and water molecules adsorbed on the surface of the materials. Bands were also observed at 1054 cm^{-1}, 993 cm^{-1}, 862 cm^{-1} and 610 cm^{-1}, which are attributed, respectively, to (C–O–C) asymmetric valence vibration of the cellulose pyran ring, other vibrations of the pyran ring, asymmetric deformations of the HPO_4^{2-} group (P-O-(H)) and asymmetric deformation of PO_4^{3-}. Regarding the occurrence of bands referring to cerium, several researchers report the appearance of multiple bands between 800 and 400 cm^{-1}. The characteristic band of rare earth phonic modes appeared at around 558 cm^{-1}. A band indicative of Ce-O stretching was observed at 535 cm^{-1}, as shown in Fig. 2e [49]. The obtained spectra revealed that the biomaterials development process did not cause significant alterations in the peaks within the FTIR spectral region when comparing the spectra of BNC, BNC-CaP, and BNC-Ce:CaP. Based on these results, it can be concluded that the functional groups of the materials used in the biomaterial development remained unchanged.

To qualitatively evaluate the crystalline phases present in the samples, diffraction analysis was performed, as illustrated in Fig. 2f. The presence of one phase for BNC (two peaks referring to bacterial nanocellulose) are shown. Similarly to Saska et al. [30], two peaks characteristic of cellulose were observed at $2\theta = \sim 15°$ and 22.7°, which were attributed to cellulose Iα and Iβ and some peaks referring to HAp, $Ca_5(PO_4)_3OH$, such as at $2\theta = 31,7°$ (high intensity), 45° and 46°, which are observed for the crystallographic record ICSD (Inorganic Crystal Structure Database) 022059 or ICDD (International Center for Diffraction Data) 01-073-0293.

Regarding the BNC-CaP composite, as shown in Figure, BNC diffraction peaks at $2\theta = 15°$ and $2\theta = 22.7°$ were not observed. Several authors report the reduction or disappearance of these peaks, given that, during the mineralization process, the BNC nanofibers are coated with a large amount of calcium phosphates [30]. The BNC-CaP diffraction profile is attributed to the occurrence of three phases: monetite, $CaHPO_4$ (ICDD 01-070-0359), in greater proportion, characterized by peaks 2θ: 13°; 26.3°; 29.8°; 30.1°; 31.4°; 31.6°; 32.1°; 45.3°, among others of lower relative intensity, hydroxyapatite, $Ca_5(PO_4)_3(OH)$ (ICDD 01–073–0293), characterized by peaks at 2θ: 25.2°; 26°; 28.4°; 31.6°; 32.1°; 45.3°; 56.4°; 68.7° and sodium chloride, NaCl (ICDD 01-078-0751), with good correlation mainly with the peaks at 2θ: 35.7° and 45.4° [24].

For the BNC-Ce:CaP composite, the occurrence of peaks characteristic of bacterial cellulose was recorded at $2\theta \sim 15°$ and at $2\theta = 22.7°$, with a lower intensity compared to BNC. The presence of monetite phase was verified (ICDD 01-070-0359), which stand out at $2\theta = 20.1°$; 26.6°; 27.3°; 31.1° and 34.6°, hydroxyapatite (ICDD 01–073–0293), with the indexation of the following peaks $2\theta = 10.5°$; 16.8°; 22.6°; 29.2°; 37.8°; 42° and 48.5°; and the brushite phase, $CaHPO_4.2H_2O$ (ICDD 00-011-0293), among which the peaks at $2\theta = 29.2°$ stand out; 31.1°; 31.7°; 33.5°; 36.5°, among others [50,51].

3.2. Cell viability

MTT method, a colorimetric assay that provides information about cytotoxicity and expresses it in terms of cellular viability, was employed for all the samples synthesized in this work [52]. As recommended by ISO 10993-5, samples with cellular viability equal to or less than 70 % are considered cytotoxic [28].

Fig. 3 presents the cell viability results for the samples, as well as for the positive (0 % cell viability) and negative (100 % cell viability) controls. BNC, BNC-CaP and BNC-Ce:CaP showed cell viability greater than 70 % and were therefore considered non-cytotoxic in relation to GM07492 fibroblast cells.

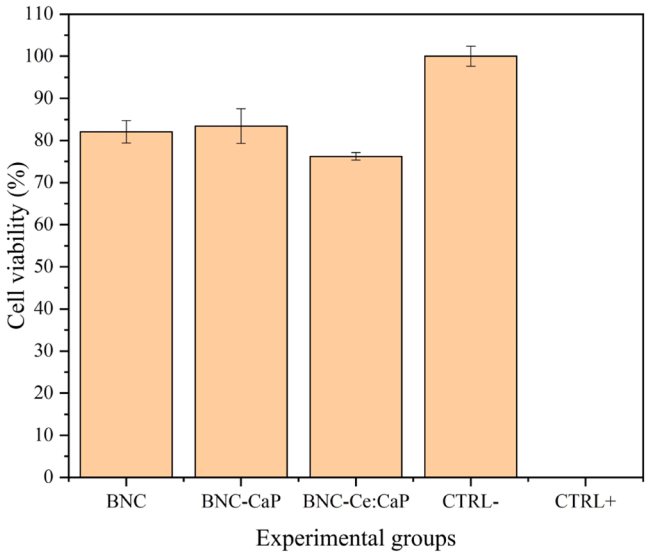

Fig. 3. Cell viability of the samples synthesized in this work.

3.3. Histomorphometric analysis

Fig. 4 presents photomicrograph at 200x magnification to demonstrate histological images used for histomorphometric evaluation (Fig. 5). It is possible to observe loose Connective Tissue (LCT), Dense Connective Tissue (DCT), Osteoid Tissue (OT), Mineralized Tissue (MT) and also the presence of the membranes (BM) in all groups after 30 and 60 day. The blue staining is a result of the tissue formation, while the red staining is related to blood clot and the white the membranes (BM). It is observed the evolution of new bone tissue from day 30 to day 60 in BNC-CaP and BNC-Ce:CaP groups.

BNC presented higher percentage of loose connective tissue (around 18 %) compare to BNC-CaP (6 %) and BNC-Ce:CaP (2 %) groups (Fig. 5a), but lower dense connective tissue after 30 days, (22 %, 45 % and 40 %, respectively). After 60 days, BNC-Ce:CaP group presented a higher percentage of dense connective tissue (35 %) compared to the other groups (both around 10 %) (Fig. 5b). BNC and BNC-CaP demonstrated differences in osteoid tissue compared to BNC-Ce:CaP, around 18 %, 20 % and 8 %, respectively, after 60 days, once after 30 days all three groups presented similar to each other (Fig. 5c). Interestingly and not expected, after both time points, BNC and BNC-Ce:CaP demonstrated a higher percentage of mineralized tissue, as observed in Fig. 5d.

3.4. Evaluation of gene expression (RT-qPCR)

The results of the gene analysis provide significant insights into the molecular mechanisms underlying bone regeneration induced by different treatments and are presented in Fig. 6. When evaluating genes associated with osteogenesis, distinct expression patterns were observed over time. On the 30th day, the expression of the Runx-2 gene was higher in the BNC-CaP group, despite the lack of statistically significant difference, while on the 60th day, all groups showed similar expression of this gene. The higher expression of the Runx-2 gene suggests a possible early induction of osteoblastic differentiation.

As for the Osterix gene, there was a statistically significant difference among the analyzed groups, with particular emphasis on the BNC group, although this difference was not maintained at the 60-day, once all groups showed similar gene expression. Osterix regulates the expression of genes involved in bone matrix synthesis and mineralization. The higher gene expression in the BNC group after 30 days could explain the greater mineralized tissue observed, once its expression is generally associated with increased osteoblastic activity.

The increased expression of Bmp-2 in the BNC-CaP and BNC-Ce:CaP

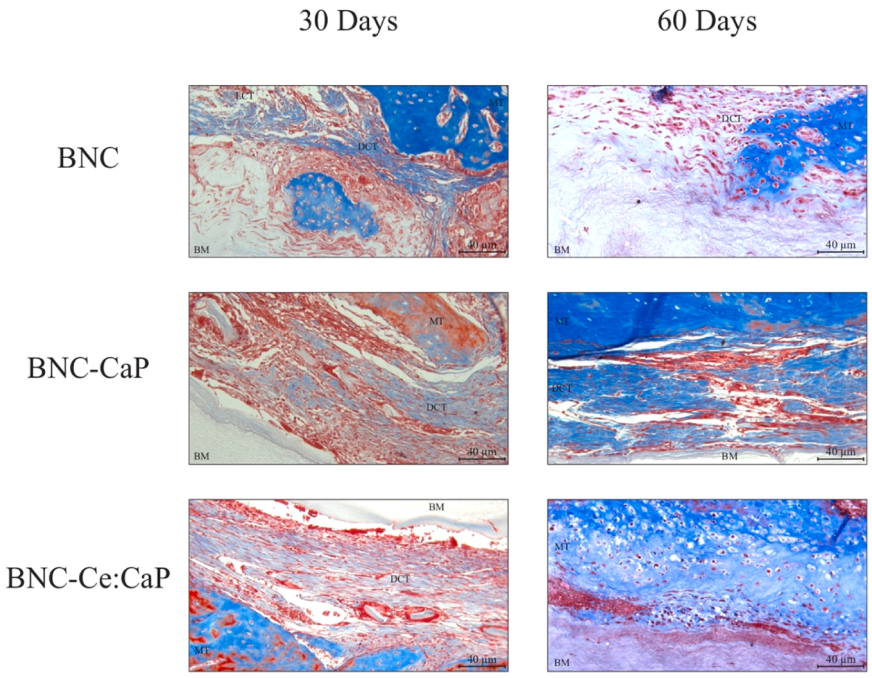

Fig. 4. Photomicrograph at 200 × magnification showing the types of tissue formed and their classification as Loose Connective Tissue (LCT), Dense Connective Tissue(DCT), Osteoid Tissue(OT), Mineralized Tissue(MT) in all groups after 30 and 60 days, stained with Masson's Trichrome.

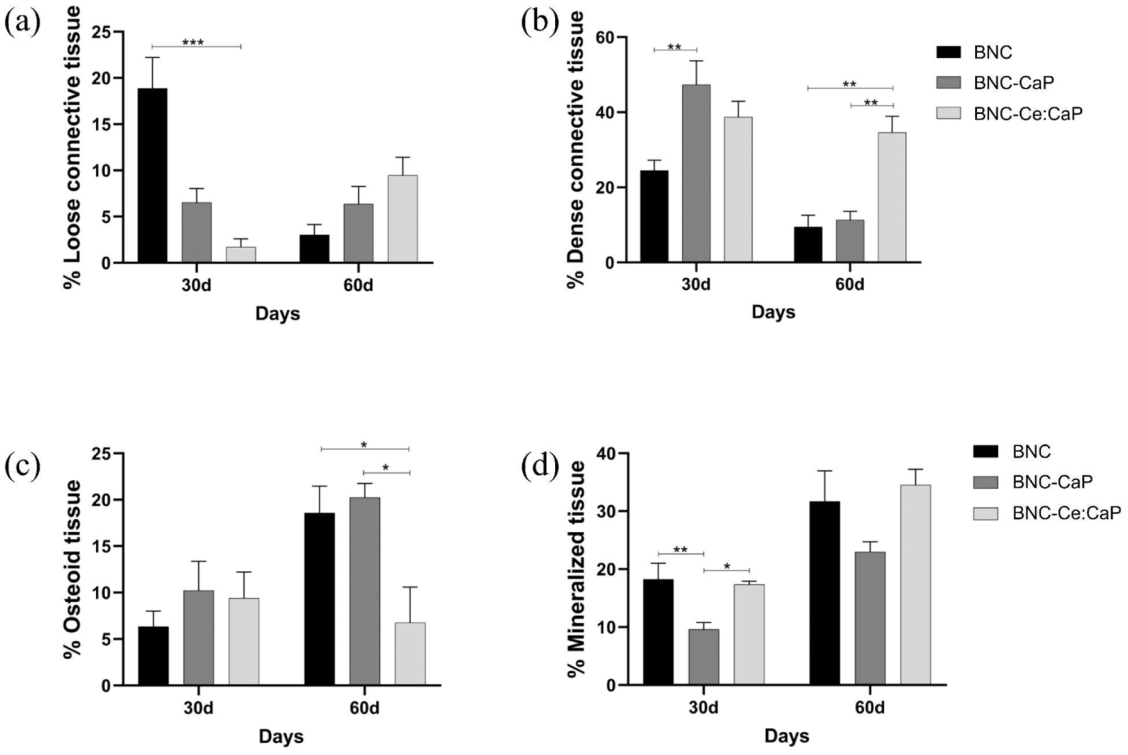

Fig. 5. Evaluation of tissue formation (histomorphometry) through the percentage of (a) loose connective tissue, (b) dense connective tissue, (c) osteoid tissue, and (d) mineralized bone tissue in all groups after 30 and 60 days. Masson's Trichrome-stained images at 200× magnification were used for quantification.

groups on the 30th and 60th days suggests a positive impact of these treatments on bone growth and differentiation signaling. The statistical difference observed on the 60th day between the BNC and BNC-CaP groups further reinforces the potential efficacy of BNC-CaP.

On the other hand, although there was a trend of higher Vegf gene expression in the BNC-CaP and BNC-Ce:CaP groups on the 30th day, no statistical difference was observed. Even though the use of cerium may participate in specific processes to assist bone differentiation [20,22], the results did not point to its influence on the tissue formation process. However, it was possible to observe the role of CaP on the process, as observed in Runx-2, Bmp-2 Vegf genes expression. In-depth analysis of Vegf gene expression may provide additional insights into the

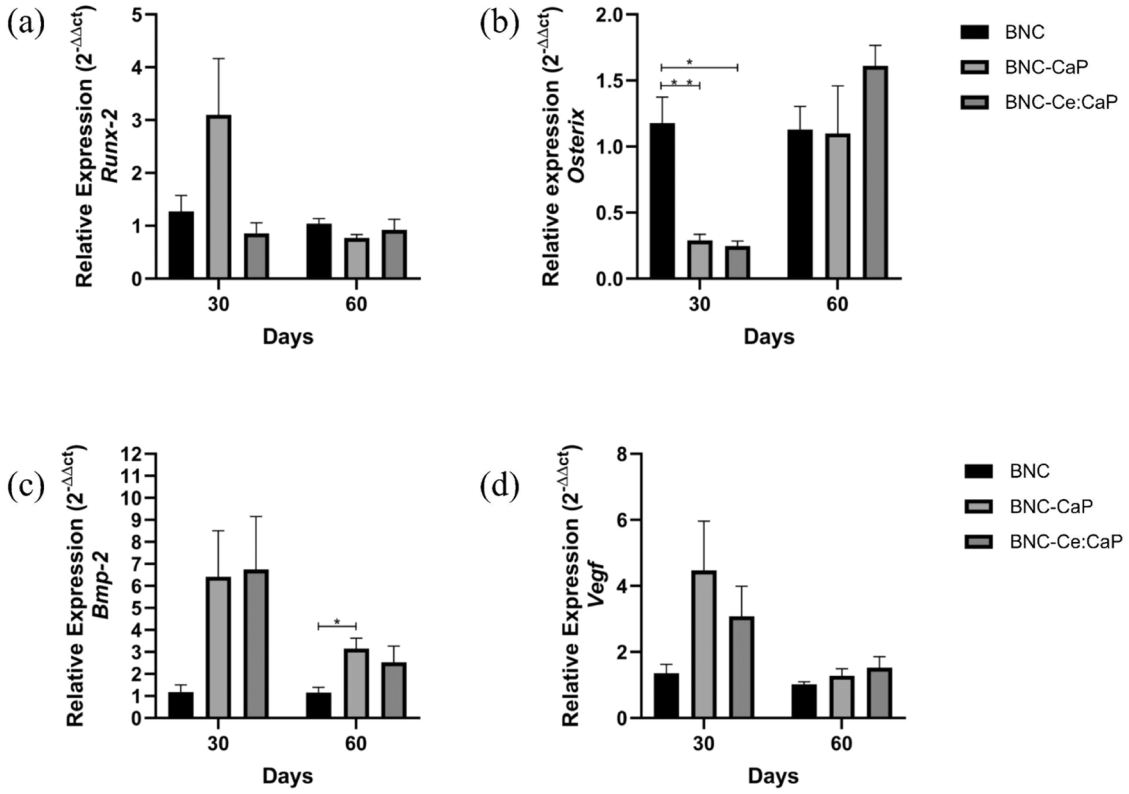

Fig. 6. Relative evaluation of the expression of osteogenic genes (a) Runx-2, (b) Osterix, (c) Bmp-2, and pro-angiogenic, (d) Vegf in all groups after 30 and 60 days.

mechanisms underlying vascularization in different treatment groups. It is important to consider that Vegf gene expression is multifaceted and can be regulated by various factors.

After 30 and 60 days, the BNC-CaP and BNC-Ce:CaP groups exhibited lower expression of the MPO gene compared to the BNC group (Fig. 7). It is possible to infer the use of CaP and/or cerium modulates the inflammatory response related to myeloperoxidase enzyme. The presence of cerium, as cerium nanoparticles have the potential to enhance the healing process of various tissues, attributed to their excellent biological properties, including antioxidant, anti-inflammatory, and antibacterial activities [22]. Regarding the CD86 gene, higher expression was observed in the BNC-CaP and BNC-Ce:CaP groups compared to the BNC group on the 30th day. However, this difference did not persist until the 60-day period. The higher CD86 expression suggests a more pronounced initial immune response [23], but this response may decrease over time, once the healing process proceeds.

The BNC-CaP and BNC-Ce:CaP groups showed higher expression of the IL1-β and IL1-RN genes on the 30th day compared to the BNC group. However, by the 60th day, the expression of the IL1-β gene reduced and became similar across the groups, while the BNC-Ce:CaP group maintained high expression of IL1-RN. This temporal change suggests a possible attenuation of the inflammatory response in the BNC-CaP and BNC-Ce:CaP groups compared to the BNC group. After 60 days, it is interesting the role of cerium as an anti-inflammatory and protective factor.

It is noteworthy that, at both 30 and 60 days, the expression of the Arg-1 gene was higher in the BNC-CaP group, even without identifying statistically significant differences. This suggests a potential for anti-inflammatory modulation in this group. These variations in gene expression patterns over time among the groups demonstrate the complex dynamics of genetic responses during the course of the experiment.

4. Conclusion

Bacterial nanocellulose (BNC), as well as bacterial nanocellulose/calcium phosphates (BNC-CaP) and cerium-containing bacterial nanocellulose/calcium phosphate composites (BNC-Ce) were investigated for cell viability. The results indicated that the composites are not cytotoxic, demonstrating adequate cell viability. During testing, no significant changes in the mass of the compounds were observed, but variations in the morphologies of the precipitated materials were noted. X-ray diffraction analysis revealed the presence of monetite (in greater proportion) and hydroxyapatite (in lesser proportion) in varying proportions in the BNC-CaP composite, while the BNC-Ce composite presented, in addition to these phases, brushite as well. Based on XPS analysis, cerium (III) is found in BNC-Ce at a concentration of 4.14 % (mol/mol).

In vivo studies showed that BNC-CaP and BNC-Ce composites played a significant role in bone tissue formation. This finding is supported by the development of mineralized tissue along with an increase in the expression of genes associated with osteogenesis, such as Osterix, angiogenic genes like Vegf, and the Bmp-2 gene, suggesting a positive impact of these treatments on bone growth and differentiation. The BNC-Ce group also demonstrated a more pronounced protective immune response, as indicated by the expression of CD86 and Il1-Rn genes. However, it is important to note that BNC-CaP showed superior results in a different scenario, highlighting the complexity of the factors at play and the need for more comprehensive analysis.

BNC-CaP produced better results, thus emphasizing the imperative to thoroughly explore BNC-CaP treatment options. Additionally, it is crucial to recognize that this study identifies its own limitations. While the results provide valuable insights into the potential of the materials studied, there is a clear need for further research to fully explore their efficacy in different clinical contexts. Possible areas for future investigation may include more extensive comparative studies between different material compositions, more detailed evaluations of the

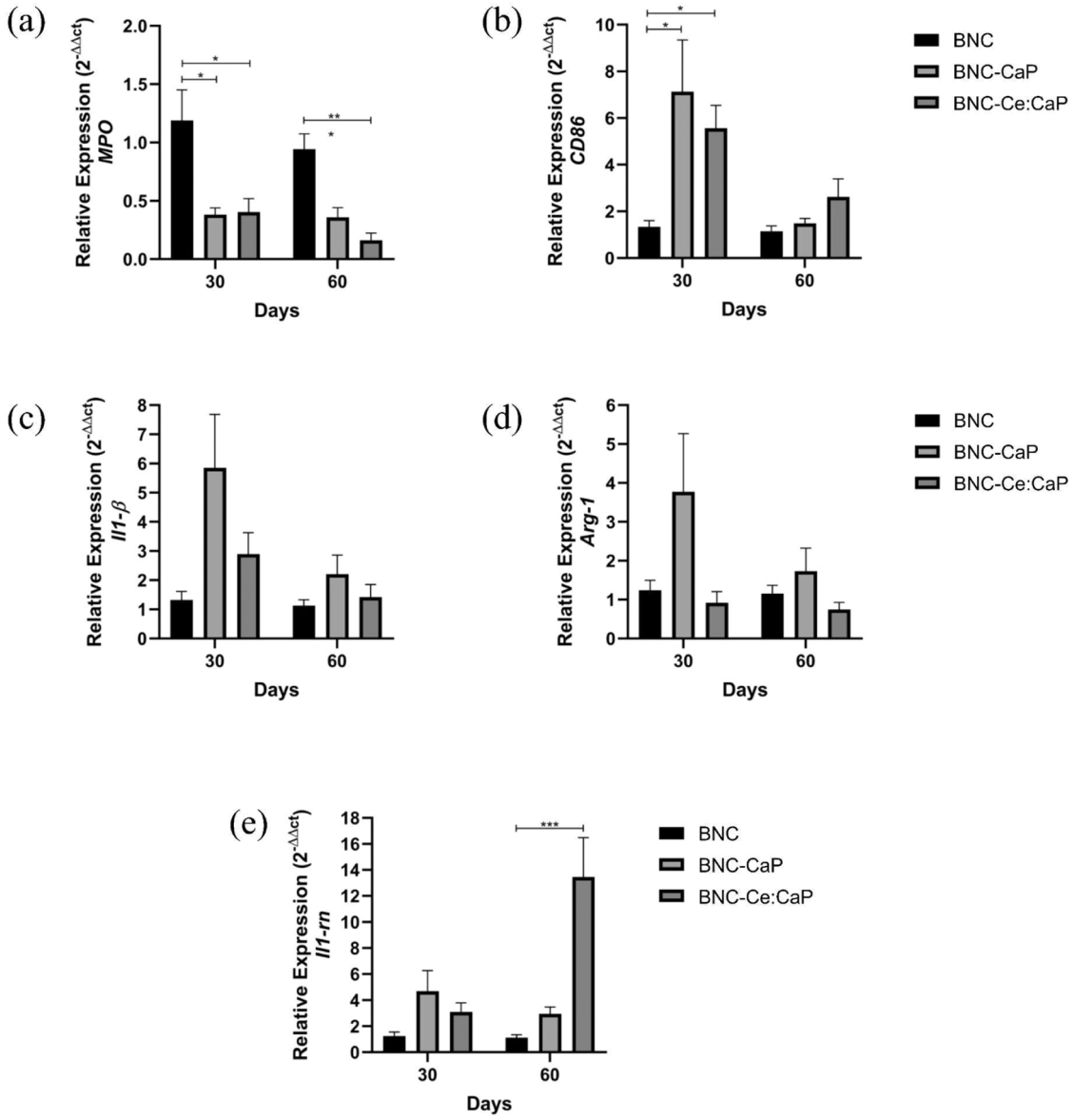

Fig. 7. Relative evaluation of the expression of inflammatory genes (a) MPO, (b) CD86, (c) IL1-β, and inhibitors of the inflammatory response, (d) Arg-1 and D) Il1-rn in all groups after 30 and 60 days.

mechanisms underlying the observed effects, and investigations into the long-term interaction of the compounds with the biological environment.

CRediT authorship contribution statement

Josy Anteveli Osajima Furtini: Writing – review & editing, Conceptualization. **Guilherme Ferreira Caetano:** Writing – review & editing, Supervision, Resources, Methodology, Formal analysis, Conceptualization. **Hernane S. Barud:** Writing – review & editing, Supervision, Resources, Methodology, Funding acquisition, Formal analysis, Conceptualization. **Edson C. Silva-Filho:** Writing – review & editing, Supervision, Resources, Methodology, Formal analysis, Conceptualization. **Gabriela Fontana de Mesquita:** Methodology, Investigation, Formal analysis, Data curation. **Pedro Henrique Ricardo:** Methodology, Investigation, Formal analysis, Data curation. **Júlia Venturini Helaehil:** Methodology, Investigation. **Santiago Medina-Carrasco:** Formal analysis, Data curation. **Ricardo Barbosa de Sousa:** Writing – original draft, Visualization, Methodology, Investigation, Formal analysis, Conceptualization. **Alessandra Cristina Dametto:** Writing – original draft, Visualization, Investigation, Formal analysis, Data curation.

Declaration of Competing Interest

The authors declare that they have no known competing financial interests or personal relationships that could have appeared to influence the work reported in this paper.

Acknowledgements

This work was supported by the National Council for Scientific and Technological Development CNPq (Grant number: 309614/2021-0) INCT-INFO (National Institute of Photonics), INCT/Polysaccharides (National Technology Science Institute for Polysaccharides), and Anton Paar. The authors thank the Coordination for improving Higher Education Personnel – CAPES and the Piauí State Research Support Foundation – FAPEPI.

Appendix A. Supporting information

Supplementary data associated with this article can be found in the online version at doi:10.1016/j.colsurfb.2024.114476.

Data availability

Data will be made available on request.

References

[1] R. Khalid, M. Khan, T. Ul-Islam, F. Khan, Wahid, Bacterial cellulose-zinc oxide nanocomposites as a novel dressing system for burn wounds, Carbohydr. Polym. 164 (2017) 214–221, https://doi.org/10.1016/j.carbpol.2017.01.061.

[2] G.F. Picheth, C.L. Pirich, M.R. Sierakowski, M.A. Woehl, C.N. Sakakibara, C. F. Souza, A.A. Martin, R. Silva, R.A. Freitas, Bacterial cellulose in biomedical applications: a review, Int. J. Biol. Macromol. 104 (2017) 97–106, https://doi.org/10.1016/j.ijbiomac.2017.05.171.

[3] E.E. Kalyoncu, E. Peşman, Bacterial cellulose as reinforcement in paper made from recycled office waste pulp, BioRes 15 (2020) 8496, https://doi.org/10.15376/biores.15.4.8496-8514.

[4] S. Gorgieva, J. Trček, Bacterial cellulose: production, modification and perspectives in biomedical applications, Nanomater 9 (2019) 1352, https://doi.org/10.3390/nano9101352.

[5] P. Basu, N. Saha, R. Alexandrova, P. Saha, Calcium phosphate incorporated bacterial cellulose-polyvinylpyrrolidone based hydrogel scaffold: structural property and cell viability study for bone regeneration application, Polymers 11 (2019) 1821, https://doi.org/10.3390/polym11111821.

[6] F.K. Andrade, N. Alexandre, I. Amorim, F. Gartner, A.C. Maurício, A.L. Luís, M. Gama, Studies on the biocompatibility of bacterial cellulose, J. Bioact. Compat. Polym. 28 (2013) 97–112, https://doi.org/10.1177/0883911512467643.

[7] W. Liu, H. Du, M. Zhang, K. Liu, H. Liu, H. Xie, X. Zhang, C. Si, Bacterial cellulose-based composite scaffolds for biomedical applications: a review, ACS Sustain. Chem. Eng. 8 (2020) 7536–7562, https://doi.org/10.1021/acssuschemeng.0c00125.

[8] R.B. Sousa, A.C. Dametto, R.M. Sabio, R.A. Carvalho, E.G. Vieira, A.F.A. Oliveira, L. K. Ribeiro, H.S. Barud, E.C. Silva-Filho, Cerium-doped calcium phosphates precipitated on bacterial cellulose platform by mineralization, Ceram. Int. 46 (2020) 26985–26990, https://doi.org/10.1016/j.ceramint.2020.07.175.

[9] M. Badshah, H. Ullah, F. He, F. Wahid, U. Farooq, M. Anderson, M., T. Khan, Development and evaluation of drug loaded regenerated bacterial cellulose-based matrices as a potential dosage form, Front. Bioeng. Biotechnol. 8 (2020) 1–10.

[10] N.V. Lukasheva, D.A. Tolmachev, Cellulose nanofibrils and mechanism of their mineralization in biomimetic synthesis of hydroxyapatite/native bacterial cellulose nanocomposites: molecular dynamics simulations, Langmuir 32 (2016) 125–134, https://doi.org/10.1021/acs.langmuir.5b03953.

[11] M. Ul-Islam, T. Khan, J.K. Park, Water holding and release properties of bacterial cellulose obtained by in situ and ex situ modification, Carbohydr. Polym. 88 (2012) 596–603, https://doi.org/10.1016/j.carbpol.2012.01.006.

[12] S. Ustunel, M.E. Prévôt, G.A.R. Rohaley, R.W. Caitlyn, B. Yavitt, G. Freychet, M. Zhernenkov, R. Pindak, E. Schaible, C. Zhu, T. Hegmann, R.J. Clements, E. Hegmann, Mechanically tunable elastomer and cellulose nanocrystal composites as scaffolds for in vitro cell studies, Mater. Adv. 2 (2021) 464–476, https://doi.org/10.1039/D0MA00676A.

[13] E.M. Fernandes, R.A. Pires, J.F. Mano, R.L. Reis, Bionanocomposites from lignocellulosic resources: properties, applications and future trends for their use in the biomedical field, Prog. Polym. Sci. 38 (2013) 1415–1441, https://doi.org/10.1016/j.progpolymsci.2013.05.013.

[14] D.A. Tolmachev, N.V. Lukasheva, Interactions binding mineral and organic phases in nanocomposites based on bacterial cellulose and calcium phosphates, Langmuir 28 (2012) 13473–13484, https://doi.org/10.1021/la302418x.

[15] M.T. Maia, E.P.C.G. Luz, F.K. Andrade, M.F. Rosa, M.F. Borges, M.R.A. Arcanjo, R. S. Vieira, Advances in bacterial cellulose/strontium apatite composites for bone applications, Polym. Rev. 61 (2021) 736–764, https://doi.org/10.1080/15583724.2021.1896543.

[16] M. Dapporto, D. Gardini, A. Tampieri, S. Sprio, Nanostructured strontium-doped calcium phosphate cements: a multifactorial design, Appl. Sci. 11 (2021) 2075, https://doi.org/10.3390/app11052075.

[17] M. Montesi, S. Panseri, M. Dapporto, A. Tampieri, S. Sprio, Sr-substituted bone cements direct mesenchymal stem cells, osteoblasts and osteoclasts fate, PLoS One 12 (2017) 1–13, https://doi.org/10.1371/journal.pone.0172100.

[18] M. Schumacher, A.S. Wagner, J. Kokesch-Himmelreich, A. Bernhardt, M. Rohnke, S. Wenisch, M. Gelinsky, Strontium substitution in apatitic CaP cements effectively attenuates osteoclastic resorption but does not inhibit osteoclastogenesis, Acta Biomater. 37 (2016) 184–194, https://doi.org/10.1016/j.actbio.2016.04.016.

[19] M.V.B. Santos, L.B.N. Rocha, E.G. Vieira, A.L. Oliveira, A.O. Lobo, M.A. M. Carvalho, J.A. Osajima, E.C. Silva-Filho, Development of composite scaffolds based on cerium doped-hydroxyapatite and natural gums - biological and mechanical properties, Mater 12 (2019) 2389–2410, https://doi.org/10.3390/ma12152389.

[20] S. Ren, Y. Zhou, K. Zheng, X. Xu, J. Yang, X. Wang, L. Miao, H. Wei, Y. Hu, Y. Xu, Cerium oxide nanoparticles loaded nanofibrous membranes promote bone regeneration for periodontal tissue engineering, Bioact. Mater. 7 (2022) 242–253, https://doi.org/10.1016/j.bioactmat.2021.05.037.

[21] D.M.D.M. Prabaharan, K. Sadaiyandi, M. Mahendran, S. Sagadevan, Structural, optical, morphological and dielectric properties of cerium oxide nanoparticles, Mater. Res. 19 (2016) 478–482, https://doi.org/10.1590/1980-5373-MR-2015-0698.

[22] A.S. Karakoti, N.A. Monteiro-Riviere, R. Aggarwal, J.P. Davis, R.J. Narayan, W. T. Self, J. Mcginnis, S. Seal, Nanoceria as antioxidant: synthesis and biomedical applications, Jom 60 (2008) 33–37, https://doi.org/10.1007/s11837-008-0029-8.

[23] S. Kargozar, F. Baino, S.J. Hoseini, S. Hamzehlou, M. Darroudi, J. Verdi, J. L. Hasanzadeh, Hae-Won Kim, M. Mozafari, Biomedical applications of nanoceria: new roles for an old player, Nanomed 13 (2018) 3051–3069, https://doi.org/10.2217/nnm-2018-0189.

[24] G. Balakrishnan, C.M. Raghavan, C. Ghosh, R. Divakar, E. Mohandas, J.I. Song, S. I. Bae, T.G. Kim, X-ray diffraction, Raman and photoluminescent studies of nanocrystalline cerium oxide thin films, Ceram. Int. 39 (2013) 8327–8333, https://doi.org/10.1016/j.ceramint.2013.03.103.

[25] P.A. Yurova, N.Y. Tabachkova, I.A. Stenina, A.B. Yaroslavtsev, Properties of ceria nanoparticles with surface modified by acidic groups, J. Nanopart. Res. 22 (2020) 318, https://doi.org/10.1007/s11051-020-05049-5.

[26] S.V. Harb, E. Kolanthai, A.S. Pugazhendhi, C.A. Beatrice, L.A. Pinto, C.J. Neal, E. H. Backes, A.C.C. Nunes, H.S.S. Araújo, L.C. Costa, M.J. Coathup, S. Seal, L. A. Pessan, 3D printed bioabsorbable composite scaffolds of poly (lactic acid)-tricalcium phosphate-ceria with osteogenic property for bone regeneration, Biomater. Biosyst. 13 (2024) 100086, https://doi.org/10.1016/j.bbiosy.2023.100086.

[27] S. Hutchens, S.A. Benson, B.R. Evans, H.M. O'Neill, C.J. Rawn, Biomimetic synthesis of calcium-deficient hydroxyapatite in a natural hydrogel, Biomater 27 (2006) 4661–4670, https://doi.org/10.1016/j.biomaterials.2006.04.032.

[28] I.I. STANDARD, ISO 10993-5, Biological Evaluation of Medical Device-Part 5: Tests for In Vitro Cytotoxicity, 2009.

[29] L.C. Junqueira, J. Carneiro, Histologia básica: texto e atlas, Guanabara-Koogan, 2018.

[30] S. Saska, H.S. Barud, A.M.M. Gaspar, R. Marchetto, S.J.L. Ribeiro, Y. Messaddeq, Bacterial cellulose-hydroxyapatite nanocomposites for bone regeneration, Int. J. Biomater. 2011 (2011) 175362, https://doi.org/10.1155/2011/175362.

[31] C. Busuioc, C.D. Ghitulica, A. Stoica, M. Stroescu, G. Voicu, V. Ionita, L. Averous, S. I. Jinga, Calcium phosphates grown on bacterial cellulose template, Ceram. Int 44 (2018) 9433–9441, https://doi.org/10.1016/j.ceramint.2018.02.160.

[32] A. Taubert, C. Balischewski, D. Hentrich, T. Elschner, S. Eidner, C. Günter, K. Behrens, T. Heinze, Water-soluble cellulose derivatives are sustainable additives for biomimetic calcium phosphate mineralization, Inorganic 4 (2016) 33, https://doi.org/10.3390/inorganics4040033.

[33] Y. Wan, G. Zuo, F. Yu, Y. Huang, K. Ren, H. Luo, Preparation and mineralization of three-dimensional carbon nanofibers from bacterial cellulose as potential scaffolds for bone tissue engineering, Surf. Coat. Technol. 205 (2011) 2938–2946, https://doi.org/10.1016/j.surfcoat.2010.11.006.

[34] L. Yang, Q. Liu, T. Liang, J. Yin, L. Qin, Y. Tang, X. Jiang, Hydrothermal synthesis of hydroxyapatite urchins and its drug release property, Adv. Mater. Res. (2011) 1681–1684, https://doi.org/10.4028/www.scientific.net/AMR.311-313.1681, 311–313.

[35] J. Li, M. Liu, Y. Qiu, Y. Gan, H. Jiang, B. Liu, H. Wei, N. Ma, Urchin-like hydroxyapatite/graphene hollow microspheres as pH-responsive bone drug carriers, Langmuir 37 (2021) 4137–4146, https://doi.org/10.1021/acs.langmuir.0c03640.

[36] F.W. Liu, B. Sun, X.Z. Jiang, S.S. Aldeyb, Q.H. Zhang, M.F. Zhu, Mechanical properties of dental resin/composite containing urchin-like hydroxyapatite, Dent. Mater. 30 (2014) 1358–1368, https://doi.org/10.1016/j.dental.2014.10.003.

[37] L. Yang, Q. Liu, T. Liang, J. Yin, L. Qin, Y. Tang, X. Jiang, Hydrothermal synthesis of hydroxyapatite urchins and its drug release property, Adv. Mater. Res. 311–313 (2011) 1681–1684, https://doi.org/10.4028/www.scientific.net/AMR.311-313.1681.

[38] G. Kumar, A. Thamizhavel, E.K. Girija, Microwave conversion of eggshells into flower-like hydroxyapatite nanostructure for biomedical applications, Mater. Lett. 76 (2012) 198–200, https://doi.org/10.1016/j.matlet.2012.02.106.

[39] C. Luo, S. Wu, J. Li, X. Li, P. Yang, G. Li, Chitosan/calcium phosphate flower-like microparticles as carriers for drug delivery platform, Int. J. Biol. Macromol. 155 (2020) 174–183, https://doi.org/10.1016/j.ijbiomac.2020.03.172.

[40] J. Wei, Z. Yang, Y. Yang, Fabrication of three dimensional CeO_2 hierarchical structures: precursor template synthesis, formation mechanism and properties, CrystEngComm 13 (2011) 2418–2424, https://doi.org/10.1039/C0CE00635A.

[41] E. Vieira, M. Silva, A. Maia-Filho, D. Ferreira, J. Figuerêdo-Silva, K. Rovaris, A. C. Fialho, A. Leite-Oliveira, A.L.M. Oliveira, M.G. Fonseca, J.A. Osajima, E.C. Silva-Filho, Effect of cerium-containing hydroxyapatite in bone repair in female rats with osteoporosis induced by ovariectomy, Minerals 11 (2021) 377, https://doi.org/10.3390/min11040377.

[42] Y. Cao, H. Zheng, G. Zhu, H. Wu, L. He, Ceria supported Ru^0-$Ru^{\delta+}$ clusters as efficient catalyst for arenes hydrogenation, Chin. Chem. Lett. (2020), https://doi.org/10.1016/j.cclet.2020.05.045.

[43] H.S. Barud, C.A. Ribeiro, M.S. Crespi, M.A.U. Martines, J. Dexpert-Ghys, R.F. C. Marques, Y. Messaddeq, S.J.L. Ribeiro, Thermal characterization of bacterial cellulose-phosphate composite membranes, J. Therm. Anal. Calorim. 87 (2007) 815–818, https://doi.org/10.1007/s10973-006-8170-5.

[44] M. Ibrahim, O. Osman, A.A. Mahmoud, Spectroscopic analyses of cellulose and chitosan: FTIR and modeling approach, J. Comput. Theor. Nanosci. 8 (2011) 117–123, https://doi.org/10.1166/jctn.2011.1668.

[45] M. Schwanninger, J.C. Rodrigues, H. Pereira, B. Hinterstoisser, Effects of short-time vibratory ball milling on the shape of FT-IR spectra of wood and cellulose, Vib. Spectrosc. 36 (2004) 23–40, https://doi.org/10.1016/j.vibspec.2004.02.003.
[46] M. Malakauskaite-Petruleviciene, Z. Stankeviciute, G. Niaura, E. Garskaite, A. Beganskiene, A. Kareiva, Characterization of sol-gel processing of calcium phosphate thin films on silicon substrate by FTIR spectroscopy, Vib. Spectrosc. 85 (2016) 16–21, https://doi.org/10.1016/j.vibspec.2016.03.023.
[47] J. Xie, C. Riley, M. Kumar, K. Chittur, FTIR/ATR study of protein adsorption and brushite transformation to hydroxyapatite, Biomaterials 23 (2002) 3609–3616, https://doi.org/10.1016/S0142-9612(02)00090-X.
[48] M. Kumar, J. Xie, K. Chittur, C. Riley, Transformation of modified brushite to hydroxyapatite in aqueous solution: effects of potassium substitution, Biomater 20 (1999) 1389–1399, https://doi.org/10.1016/s0142-9612(99)00043-5.
[49] S. Safat, F. Buazar, S. Albukhaty, S. Matroodi, Enhanced sunlight photocatalytic activity and biosafety of marine-driven synthesized cerium oxide nanoparticles, Sci. Rep. 11 (2021) 1–11, https://doi.org/10.1038/s41598-021-94327-w.
[50] M. Švecová, V. Bartůněk, Facile synthesis of monetite nanoparticles from basic raw materials, Ceram. Int. 44 (2018) 16079–16082, https://doi.org/10.1016/j.ceramint.2018.05.187.
[51] R.L. Frost, Y. Xi, Y.G. Millar, K. Tan, S.J. Palmer, Vibrational spectroscopy of natural cave mineral monetite $CaHPO_4$ and the synthetic analog, Spectrosc. Lett. 46 (2013) 54–59, https://doi.org/10.1080/00387010.2012.663852.
[52] S. Unal, S. Arslan, B.K. Yilmaz, F.N. Oktar, A.Z. Sengil, O. Gunduz, Production and characterization of bacterial cellulose scaffold and its modification with hyaluronic acid and gelatin for glioblastoma cell culture, Cellul 28 (2021) 117–132, https://doi.org/10.1007/s10570-020-03528-5.